Title

Unveiling the Role of tBP-LiTFSI Complexes in Perovskite Solar Cells.

Journal

Journal of the American Chemical Society, 140(48)

ISSN

0002-7863

Authors

Wang, Shen
Huang, Zihan
Wang, Xuefeng
et al.

Publication Date

2018-12-01

DOI

10.1021/jacs.8b09809

Peer reviewed

JACS
JOURNAL OF THE AMERICAN CHEMICAL SOCIETY
Article
Cite This: J. Am. Chem. Soc. XXXX, XXX, XXX−XXX
pubs.acs.org/JACS

Unveiling the Role of tBP−LiTFSI Complexes in Perovskite Solar Cells

Shen Wang,[†] Zihan Huang,[†] Xuefeng Wang,[†] Yingmin Li,[‡,§] Marcella Günther,[⊥] Sophia Valenzuela,[†] Pritesh Parikh,[†] Amanda Cabreros,[†] Wei Xiong,*[,‡,§] and Ying Shirley Meng*[,†,‡]

[†]Department of NanoEngineering, [‡]Materials Science and Engineering Program, and [§]Department of Chemistry and Biochemistry, University of California, San Diego, 9500 Gilman Drive, La Jolla, California 92093, United States

[⊥]Department of Chemistry and Pharmacy, University of Würzburg, Am Hubland, Campus Süd, Würzburg 97074, Germany

Supporting Information

ABSTRACT: Lead halide-based perovskite materials have been applied as an intrinsic layer for next-generation photovoltaic devices. However, the stability and performance reproducibility of perovskite solar cells (PSCs) needs to be further improved to match that of silicon photovoltaic devices before they can be commercialized. One of the major bottlenecks that hinders the improvement of device stability/reproducibility is the additives in the hole-transport layer, lithium bis(trifluoromethanesulfonyl)imide (LiTFSI) and 4-*tert*-butylpyridine (tBP). Despite the positive effects of these hole-transport layer additives, LiTFSI is hygroscopic and can adsorb moisture to accelerate the perovskite decomposition. On the other hand, tBP, the only liquid component in PSCs, which evaporates easily, is corrosive to perovskite materials. Since 2012, the empirical molar ratio 6:1 tBP:LiTFSI has been wildly applied in PSCs without further concerns. In this study, the formation of tBP−LiTFSI complexes at various molar ratios has been discovered and investigated thoroughly. These complexes in PSCs can alleviate the negative effects (decomposition and corrosion) of individual components tBP and LiTFSI while maintaining their positive effects on perovskite materials. Consequently, a minor change in tBP:LiTFSI ratio results in huge influences on the stability of perovskite. Due to the existence of uncomplexed tBP in the 6:1 tBP:LiTFSI mixture, this empirical tBP−LiTFSI molar ratio has been demonstrated not as the ideal ratio in PSCs. Instead, the 4:1 tBP:LiTFSI mixture, in which all components are complexed, shows all positive effects of the hole-transport layer components with dramatically reduced negative effects. It minimizes the hygroscopicity of LiTFSI, while lowering the evaporation speed and corrosive effect of tBP. As a result, the PSCs fabricated with this tBP:LiTFSI ratio have the highest average device efficiency and obviously decreased efficiency variation with enhanced device stability, which is proposed as the golden ratio in PSCs. Our understanding of interactions between hole-transport layer additives and perovskite on a molecular level shows the pathway to further improve the PSCs' stability and performance reproducibility to make them a step closer to large-scale manufacturing.

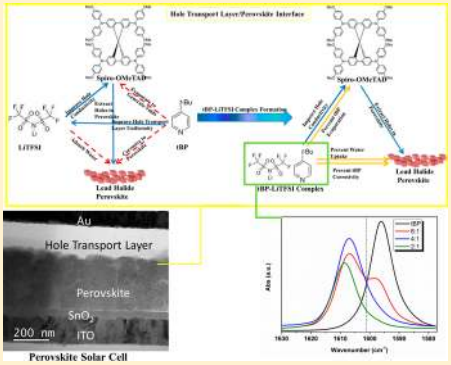

INTRODUCTION

In 2012, after Grätzel and Park et al. substituted the liquid electrolyte for a solid-state hole-transport layer in perovskite-sensitized solar cells, a rising star, lead halide perovskite materials, has risen in the energy field.[1] Nowadays, lead halide-based perovskite materials have been widely applied as core components for different types of energy conversion devices such as next-generation solar cells, X-ray detectors, light-emitting diodes, and laser generators.[1−9] For the next-generation solar cells, a power conversion efficiency (PCE) of 23.3% has been achieved using single-junction perovskite solar cells (PSCs).[10] This can be attributed to the tunable bandgap, long carrier diffusion length, and low exciton binding energy of various perovskite materials.[11−13] A PSC is a p−i−n junction device, which consists of an electron-transport layer (ETL), an intrinsic layer, and a hole-transport layer (HTL). The lead halide perovskite materials function as an intrinsic layer that can absorb photons and generate free electron−hole pairs. The electrons are transferred to the ETL, while the holes are extracted by the HTL to finish regenerating the perovskite layer.[14]

For the HTLs, organic molecules,[15−20] polymers,[21,22] and inorganic semiconductors[23−26] have all been applied for PSCs. Although some recent publications show that inorganic HTLs can achieve over 20% efficiency with better device stability,[24] the highest device performance is still based on the doped organic/polymeric HTL.[27]

The most commonly used organic and polymeric hole-transport materials in PSCs are 2,2′,7,7′-tetrakis(*N*,*N*-di-*p*-methoxyphenylamine)-9,9′-spirobifluorene (Spiro-OMeTAD) or poly[bis(4-phenyl)(2,4,6-trimethylphenyl)amine] (PTAA).[8,27,28] Bis(trifluoromethane)sulfonimide lithium salt (LiTFSI) and 4-*tert*-butylpyridine (tBP) are added to Spiro-OMeTAD or PTAA in the HTL as additives. Although LiTFSI and tBP were termed as "additives", indicating that they are

Received: September 10, 2018
Published: November 6, 2018

DOI: 10.1021/jacs.8b09809
J. Am. Chem. Soc. XXXX, XXX, XXX−XXX

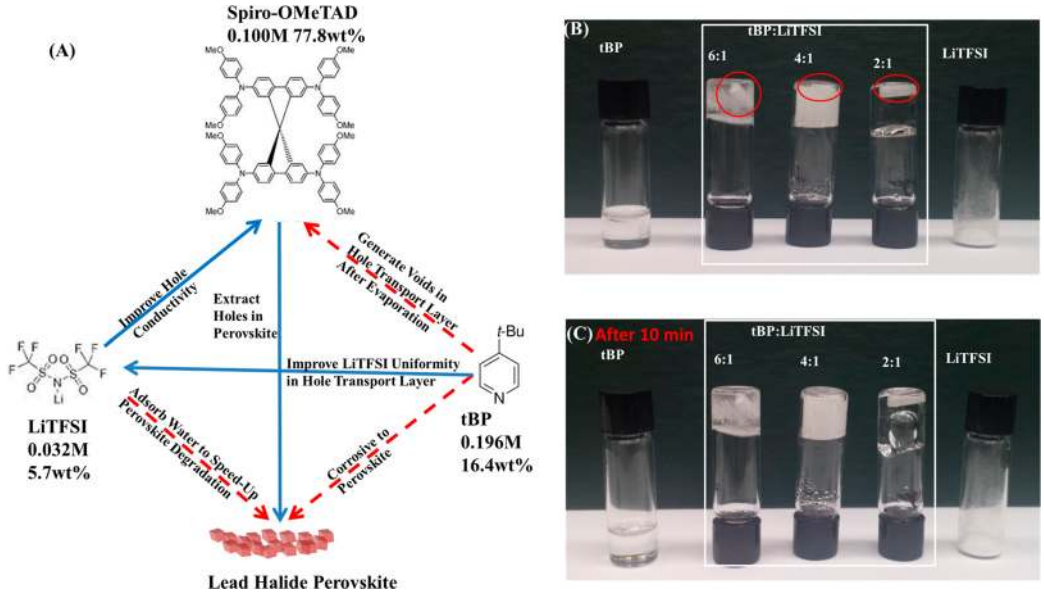

Figure 1. Hole-transport layer components and optical images of tBP–LiTFSI mixtures at different molar ratios. (A) Chemical structures of hole-transport layer components (with molar concentration and weight percentage) in perovskite solar cells and interactions between the components and perovskite (the blue solid arrows show positive effects, while the red dashed arrows show negative effects). (B) tBP–LiTFSI mixtures in vials with black lids placed upside down (stir bars in the vials are marked with red circles) and (C) after 10 min.

not the major components, on a molecular level, tBP and LiTFSI are the dominant components in HTL. Despite that in Spiro-OMeTAD-based HTL Spiro-OMeTAD accounts for ~70% (weight percentage), the molar ratio of Spiro-OMeTAD:LiTFSI:tBP is ~1:0.5:3. This means that the composition of HTL is dominated by LiTFSI and tBP, while these additives could play a significant role in the chemical environment of HTL. This evaluation is based on the commonly reported concentration condition of a Spiro-OMeTAD-based HTL solution that is made up of 122.5 mg of Spiro-OMeTAD, 17.7 μL of LiTFSI–acetonitrile solution (520 mg/mL LiTFSI in acetonitrile), and 28.8 μL of tBP in 1 mL of chlorobenzene.[8] In HTL, LiTFSI normally functions as the p-dopant, which improves the hole conductivity of this layer,[29,30] whereas tBP enhances the hole extraction on the perovskite/HTL interface.[31−33]

Although PSCs have a high energy conversion efficiency and low manufacturing cost, the low device stability limits its further application and commercialization. First, the perovskite intrinsic layer is moisture sensitive. The perovskite materials can degrade their precursors under exposure to moisture.[34−36] On the other hand, the ETL and HTL in PSCs reduce the device stability: in the ETL, TiO_2 may cause the perovskite to decompose on exposure to UV light and oxygen.[37,38] Other organic electron-transport materials such as phenyl-C61-butyric acid methyl ester (PCBM) are also oxygen sensitive.[39] As shown in our previous work, in HTL, the negative effects for the device stability are mainly from the additives LiTFSI and tBP. The LiTFSI is hygroscopic, which can adsorb water and turn into liquid in seconds in an ambiant condition. tBP, as the only liquid component in PSCs, can gradually evaporate at room temperature although its boiling point is 197 °C.[31] Moreover, tBP is corrosive to the intrinsic layer by dissolving perovskite materials.[40] These additives in HTL further reduce the stability of PSCs. Several alternative additives with improved stability in PSCs have been reported.[41,42] However, either with the lower power conversion efficiency or higher price, these additives are not suitable to substitute LiTFSI and tBP.

On the other hand, when LiTFSI and tBP coexist in PSCs, their individual negative effects on PSCs are limited. Previous studies show that the hygroscopicity of HTL induced by LiTFSI decreases when tBP exists.[31] Also, tBP controls the morphology of HTL by assisting in uniform distribution of LiTFSI in the bulk HTL solution.[29,33] Both positive and negative effects among the HTL components and perovskite are shown in Figure 1(A). However, the mechanism on why tBP improves the LiTFSI distribution in HTL has not been clarified yet. Moreover, the most commonly applied tBP:LiTFSI molar ratio in PSCs HTL is around 6:1 (for more detailed information see Supporting Information, Table S1). To our knowledge, the 6:1 tBP:LiTFSI ratio in Spiro-OMeTAD HTL was first utilized in solid-state dye-sensitized solar cells (ss-DSSCs) in 2011.[43] Since then, this combination of HTL from ss-DSSCs with fixed molar ratio and components was introduced to PSCs in 2012, the year when PSCs started to develop as a new type of solar cell.[8,9] These first several PSC works greatly influenced the following studies. As a result, a 6:1 tBP:LiTFSI was applied as the default ratio in the PSC field.

Despite the prevalence of 6:1 tBP:LiTFSI, it is unclear whether or why this ratio is ideal in PSCs. Thus, understanding the reason that the negative effects of additives in HTL are reduced when LiTFSI and tBP coexist can lead to an optimized tBP:LiTFSI ratio or a rational selection of the better alternative additive(s) to improve the PSCs' performance.

In this study, the formation of tBP–LiTFSI complexes at different molar ratios has been identified and characterized for the first time. On a molecular level, the formation of tBP–LiTFSI complexes is based on the pyridine ring in tBP coordinates with the lithium ion in LiTFSI. These complexes are more stable than individual LiTFSI and tBP in the HTL. In these complexes, the evaporation speed of tBP has been slowed down and the corrosive effect of tBP on perovskite has been restricted. The hygroscopicity of LiTFSI in these complexes is

DOI: 10.1021/jacs.8b09809
J. Am. Chem. Soc. XXXX, XXX, XXX–XXX

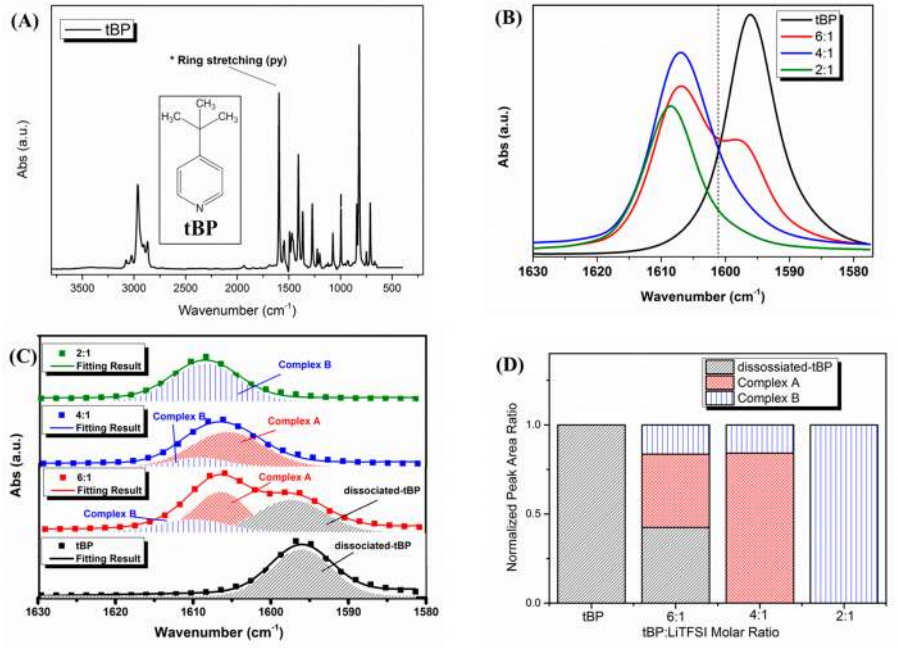

Figure 2. Fourier-transform infrared spectroscopy (FTIR) of (A) tBP with a ring stretching mode peak at 1596 cm^{-1} labeled in the figure, (B) the ring stretching mode peaks for tBP and tBP−LiTFSI mixtures at different molar ratios, (C) the fitting for the FTIR peaks of (B), and (D) the normalized peak area ratio derived from (C).

limited compared to the individual LiTFSI. Moreover, the degradation speed of perovskite to its precursors and other products is hindered as well. Based on this study, in PSCs, the optimized tBP:LiTFSI molar ratio is 4:1, which shows better device stability, less hysteresis, and less variation in power conversion efficiency. The understanding of interactions between tBP and LiTFSI shows pathways to further enhance the PSCs' performances and large-scale fabrications.

RESULTS AND DISCUSSION

Formation of tBP−LiTFSI Complexes. To identify the formation of tBP−LiTFSI complexes, tBP and LiTFSI at various molar ratios were mixed together (for the molecular structures of tBP and LiTFSI, see Figure 1(A)). At room temperature, tBP is liquid while LiTFSI is in a solid state. It was observed that 2:1 is the lowest tBP to LiTFSI molar ratio at which a homogenized mixture can be obtained. In a 1:1 tBP−LiTFSI mixture, LiTFSI cannot be fully dissolved in tBP. In most publications that used tBP−LiTFSI as the HTL additives, 6:1 was adopted as the tBP:LiTFSI ratio. Thus, the molar ratio of tBP:LiTFSI in this work focuses on the range from 6:1 to 2:1. As shown below, the 6:1, 4:1, and 2:1 mixtures have some distinguishable physical properties. The 3:1 and 5:1 mixtures had been synthesized as well, and their morphology is summarized in Supporting Information, Figure S1.

The three tBP−LiTFSI mixtures have distinguishable appearances: the 6:1 mixture forms a gel (with extra liquid, which can wet the weighing paper; see Supporting Information, Figure S1(C)), the 4:1 mixture is wax-like (without an excess amount of "free" liquid), while the 2:1 mixture forms a viscous liquid. Figure 1(B) displays these tBP−LiTFSI mixtures synthesized in black-lid glass vials with stir bars. All of the mixtures can be placed upside down to hold the stir bars. After 10 min, in Figure 1(C), no change had been observed for the 6:1 and 4:1 mixtures. However, the shape of the 2:1 mixture changed, which indicated a viscous flow-like behavior of the tBP−LiTFSI mixture at the molar ratio of 2:1. Intuitively, if the solid salt and liquid organics can be homogeneously mixed with little intermolecular interactions, it would form either a solution or quasi-solid-state gel. However, only the 6:1 mixture meets this expectation. By decreasing the tBP−LiTFSI ratio to 4:1, the wax-like material was obtained. This sample can be placed on weighing paper without wetting the paper, as shown in Supporting Information, Figure S1 (E). A further decrease in the tBP content to 2:1 (tBP−LiTFSI mixture) displayed a flow-like behavior, which was confirmed in Supporting Information, Figure S1 (G). The mixture was loaded on a metal tip, and a continuous stream is seen between the tip and stage. Among these mixtures, the 2:1 sample has the highest LiTFSI content, which should inherit its solid-state-like behavior. However, unlike the 6:1 and 4:1 samples, it appears to be a transparent liquid. This abnormal phenomenon was observed in urea−LiTFSI mixtures as well,[44] which can be attributed to the molar ratio of 2:1 being the eutectic ratio of the tBP−LiTFSI mixtures at room temperature.

Fourier-transform infrared spectroscopy (FTIR) had been applied in energy storage and conversion devices such as a lithium ion battery to identify the formation of a Li complex in their electrolytes.[45,46] This inspired us to apply FTIR to characterize the formation of tBP−LiTFSI complexes in perovskite solar cells since all of the tBP-LiTFSI mixtures are amorphous organics. Figure 2(A) is the full-range tBP FTIR. The pyridine ring stretching mode peak at ∼1596 cm^{-1} in Figure 2(A) was labeled and selected to conduct the further data analysis. The reason for focusing on this ring mode peak was that it is very sensitive to changes of conjugated π electronic orbitals of tBP upon formation of different complexes. Furthermore, the ring mode is strong and far away from vibrational modes of LiTFSI and other modes of tBP, which provides the best observation window for this study

DOI: 10.1021/jacs.8b09809
J. Am. Chem. Soc. XXXX, XXX, XXX−XXX

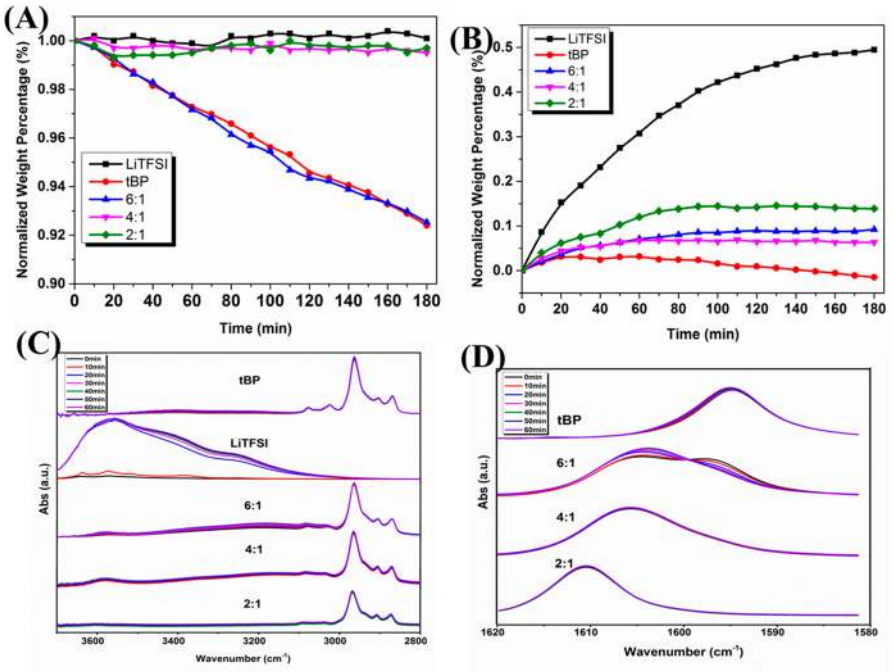

Figure 3. Evaporation and hygroscopicity of tBP, LiTFSI, and tBP−LiTFSI mixtures. Normalized weight percentage curve within 180 min: (A) tBP evaporation curve and (B) water uptake curve. FTIR of samples in an ambient condition within 60 min at (C) −OH association peak region and (D) pyridine ring stretching region.

(for the tBP FTIR with all labeled peaks see Supporting Information, Figure S2.).

As shown in Figure 2(B), the ring stretching mode peaks for tBP and tBP−LiTFSI mixtures at different molar ratios displayed different peak shapes and positions. Pure tBP only has a single peak in this region, so does the 4:1 and 2:1 tBP−LiTFSI mixtures. However, both the 4:1 and the 2:1 peak have a blue-shift. On the other hand, the spectrum of the 6:1 tBP−LiTFSI mixture shows two peaks, one close to the blue-shifted peak observed in the 4:1 and 2:1 ratio mixtures, whereas a shoulder peak appears near the peak of pure tBP liquid. (More FTIR results were collected for the tBP−LiTFSI mixtures whose molar ratios are between 1:1 and 1:10; see Supporting Information, Figure S3.) Compared with pure tBP, a clear trend was observed: With more LiTFSI added into tBP, the peak at 1596 cm^{-1} was reduced. At the same time, the peak of the blue-shifted region gradually converted into a single peak without any shoulder signal.

Previous literature shows that the nitrogen of the pyridine ring can coordinate with metal ions. There are two possible interactions between the pyridine ring and Li^+: The first interaction is the lone electron pair (on nitrogen)−Li^+ interaction, and the second one is the π electrons (on pyridine ring)−Li^+ interaction (the interactions are shown in Supporting Information, Figure S4). For the first interaction, after donating the lone electron pair, the electronegativity of nitrogen in the pyridine ring is impaired and the aromatic property of the pyridine ring is enhanced. As a result, the bond strength of the pyridine ring is enhanced, and thus the blue-shift in FTIR is expected.[47] On the other hand, the π electrons−Li^+ interaction can impair the aromatic properties of the pyridine ring; thus a red-shift of the ring stretching peak in FTIR will be observed. Because a blue-shift of the mixtures is observed (Figure 2(B)), it indicates that the formation of a tBP−LiTFSI complex is based on the Li^+−N lone electron pair interaction.

In Figure 2(B), the position of the shoulder of the 6:1 mixture matches the peak position of pure tBP, while the major peak position of the 6:1 mixture is close to the peak of the 4:1 mixture. This result explains why in Figure 1(B) and (C) the 6:1 mixture has a gel-like appearance: The extra liquid component is the tBP that does not form a complex, while the solid component forms the tBP−LiTFSI complex. In this case, a dashed line was drawn to separate Figure 2(B) into two parts: The right side of the dashed line is the uncomplexed tBP region and the left side is the complexed tBP region.

To further identify which complexes exist in these mixtures, the FTIR in Figure 2(B) was fitted as displayed in Figure 2(C). Three Gaussian peaks (1596, 1606, and 1610 cm^{-1}) were applied for fitting. The fitting results are corroborated by the experimental data. The ratio of the mixtures in the fitting peaks area is shown in Figure 2(D). The 1596 cm^{-1} peak corresponds to the uncomplexed tBP since it coincides with the pure tBP peak. The 1606 and 1610 cm^{-1} peaks reflect formation of tBP−LiTFSI complexes. These two distinct peaks could be due to either different tBP coordination numbers to Li^+ or different chemical environment-induced peak shift. In this study, the 1606 cm^{-1} peak is referred to as complex A and the 1610 cm^{-1} peak is referred to as complex B. As summarized in Figure 2(C), the ratio between complexed and uncomplexed tBP increases when the mixtures are varied from 6:1 to 2:1 ratio. Complexed and uncomplexed tBP coexist in the 6:1 and 5:1 mixtures (see Supporting Information, Figure S5). In contrast, there is only complexed tBP in the 4:1 mixture, where complex A is the dominant part in this mixture with small amount of complex B. As the ratio decrease to 3:1, there is more complex B (see Supporting Information, Figure S5), and for the 2:1 mixture, only complex B was observed. Thus, the 4:1 tBP:LiTFSI is the maximum ratio among these

DOI: 10.1021/jacs.8b09809
J. Am. Chem. Soc. XXXX, XXX, XXX−XXX

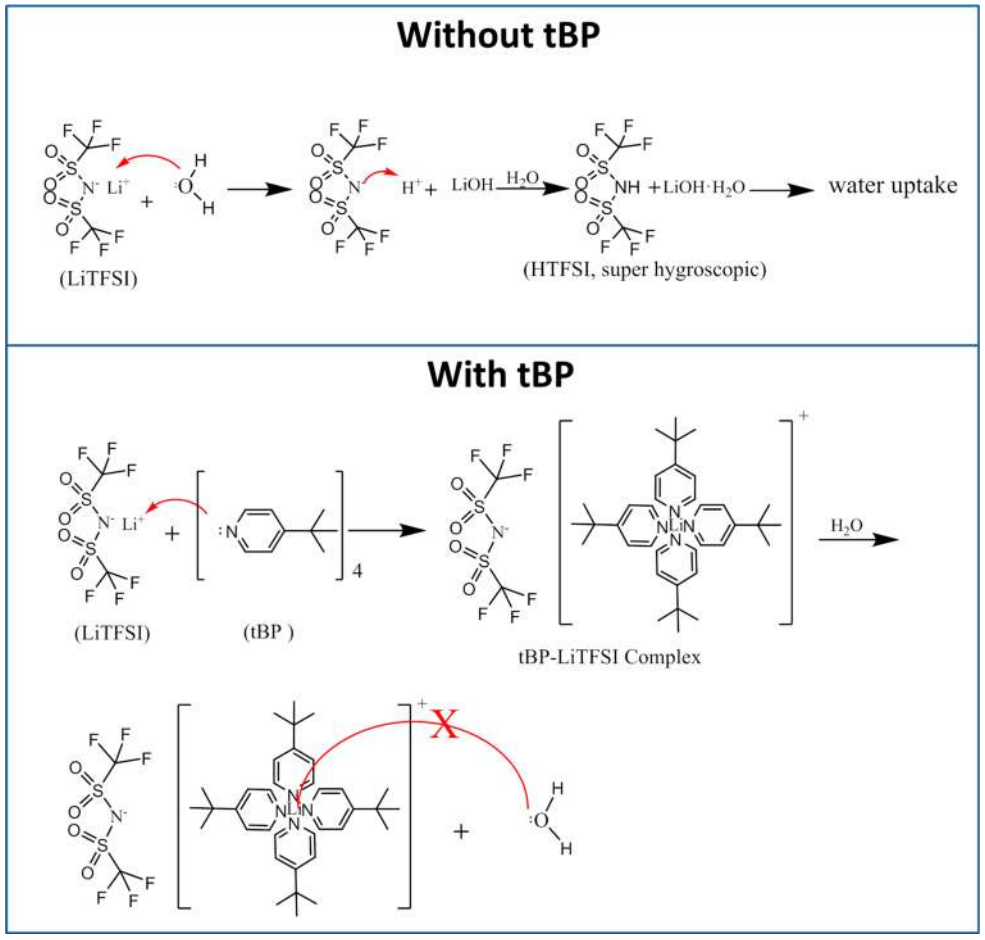

Figure 4. Proposed mechanism for how the formation of a tBP−LiTFSI complex limits water uptake.

mixtures which does not have uncomplexed tBP. This could be attributed to that 4 is the maximum number of unoccupied orbitals for Li^+ (one 2s and three 2p orbitals) to accept donated lone electron pairs. In summary, the spectroscopic study suggests that tBP and LiTFSI form chemical complexes at various mixing ratios. The next question is how complexation is related to alleviating the negative effect of tBP−LiTFSI in PSCs.

Evaporation and Hygroscopicity of tBP−LiTFSI Complexes. Our previous research demonstrated that the tBP evaporation and LiTFSI hygroscopicity further reduce the stability of PSCs:[31] Several bubble-like voids were seen across the HTL due to the tBP evaporation, which enables new sites to accumulate moisture. Meanwhile, the hygroscopicity of LiTFSI also increases the moisture level in HTL. The accumulated water in HTL due to the combined effects of tBP evaporation and LiTFSI hygroscopicity causes the perovskite intrinsic layer's degradation.

The weight changes of tBP−LiTFSI mixtures were measured to evaluate their evaporation behavior and hygroscopicity. The hygroscopicity from LiTFSI can increase the sample weight, while the tBP evaporation can decrease it. Each sample was weighed at intervals of 10 min for 180 min in a glovebox (argon gas environment) and an ambient condition separately. In the inert gas environment, the water level is low enough (<0.1 ppm) to limit the hygroscopicity effect, and the tBP evaporation should be the dominant reason to cause the sample weights to change in the glovebox. On the other hand, in ambient conditions, the tBP evaporation and LiTFSI hygroscopicity effects coexist. The water uptake weighing curve can be obtained after reducing the glovebox weighing results from the ambient condition weighing results. The evaporation and water uptake curves are shown in Figure 3(A) and (B) (for purposes of simplicity, we only selectively showed results of 2:1, 4:1, and 6:1 mixtures, pure LiTFSI, and tBP here; the results for 3:1 and 5:1 mixtures and original curves for samples in ambient condition are displayed in Supporting Information, Figure S6).

Figure 3(A) displays the normalized weight percentage change of the samples in the glovebox. A significant weight loss is seen in the tBP sample (red curve in Figure 3(A)). In the meantime, there is no weight loss for the 4:1 and 2:1 mixtures, which indicates that the formation of the tBP−LiTFSI complex (A and B) can prevent tBP from evaporating. On the contrary, a weight loss in the 6:1 mixture was observed, almost the same weight loss speed as tBP itself. This agrees with the FITR result that the 6:1 mixture has uncomplexed tBP, which can evaporate.

As shown in the water uptake curve, Figure 3(B), tBP can also adsorb a small amount of water in the first 60 min (<5%). Then its weight starts to decrease, because of the water evaporation. In the later hours, its weight was even less than its original weight percentage, albeit the tBP evaporation results (in a glovebox) had been ruled out. This phenomenon can be attributed to the coevaporation effect of water and tBP in ambient condition. Among these samples which contain

DOI: 10.1021/jacs.8b09809
J. Am. Chem. Soc. XXXX, XXX, XXX−XXX

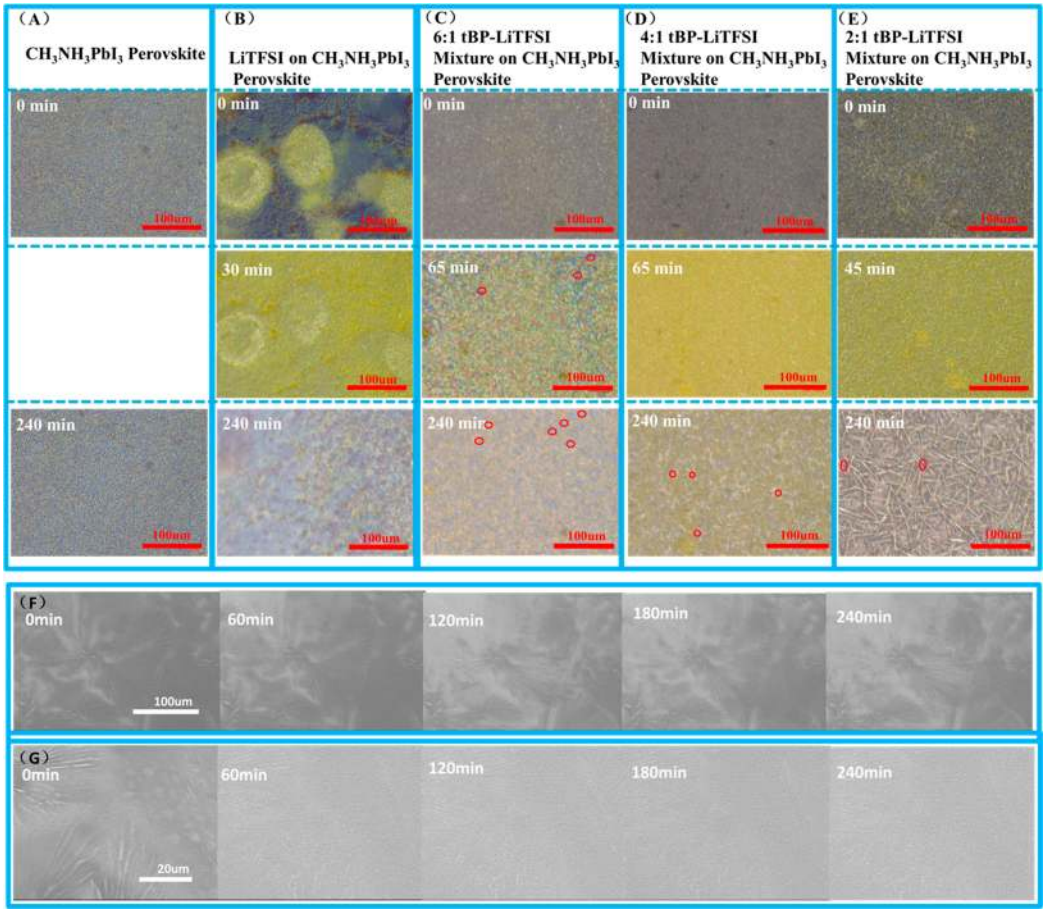

Figure 5. Optical micrographs of $CH_3NH_3PbI_3$ perovskite films exposed for 240 min in an ambient condition, which were spun with (A) nothing, (B) LiTFSI, (C) 6:1 tBP−LiTFSI mixture, (D) 4:1 tBP−LiTFSI mixture, and (E) 2:1 tBP−LiTFSI mixture. Some of the blue-colored regions were marked with red circles. Environmental scanning electron microscope (ESEM) image of $CH_3NH_3PbI_3$ perovskite films with LiTFSI under 1.1 Torr water vapor pressure for 240 min at (F) large scale and (G) small scale.

LiTFSI, the 4:1 tBP−LiTFSI mixture shows the least hygroscopicity. Even the 6:1 mixture has a higher water uptake effect than the 4:1 mixture, which could be attributed to the fact that the evaporated tBP creates more surface area in the mixture sample to adsorb water.[31] Comparing with the LiTFSI without tBP, Figure 3(B) clearly shows that the formation of tBP−LiTFSI complexes reduced the hygroscopicity of LiTFSI.

To investigate the evaporation and hygroscopicity of tBP−LiTFSI mixtures, FTIR was measured for all mixtures at various exposure times in an ambient condition as shown in Figure 3(C) and (D). Figure 3(C) displays the −OH stretch peak region (~3000 to 3700 cm^{-1}), which indicates that the samples absorbed water. There is a huge difference for LiTFSI in this region before and after the exposure for 1 h in an ambient condition. It shows that LiTFSI has strong hygroscopicity as discussed before. Two −OH stretching peaks appear in the first 10 min of LiTFSI FTIR in Figure 3(C): 3678 cm^{-1} corresponds to LiOH, while 3574 cm^{-1} is $LiOH{\cdot}H_2O$.[48] Then these two peaks were covered by a broadened peak from water later. Previous literature[49] shows that HTFSI, the conjugate acid of LiTFSI, has super-hygroscopicity and deliquescence. This means that the hydration of LiTFSI involves two steps: The Li^+ reacts with water to form LiOH first, and then the formation of HTFSI leads to more water adsorption. In contrast, for tBP and all three tBP−LiTFSI mixtures in Figure 3(C), there is no obvious −OH stretch peak here. This proves that the tBP−LiTFSI complexes mitigate the hygroscopicity of LiTFSI. According to Figure 2 and Figure 3, at the molecular level, it is clear to conclude that the coordination of the pyridine ring (tBP) with lithium ion (LiTFSI) prohibits the formation of LiOH and HTFSI, which mitigates the LiTFSI hygroscopicity. A proposed mechanism is shown in Figure 4 on how the tBP−LiTFSI (4:1 tBP−LiTFSI as the example) limits water uptake.

Unlike the transmission mode FTIR, where samples need to be dispersed in KBr, no pretreatment was done for the attenuated total reflectance FTIR sample. As a result, the concentration of tBP is 100% no matter how much it evaporates. There is no obvious change of the FTIR for the 4:1 and 2:1 samples in this range either. The unchanged peaks for the 4:1 and 2:1 mixtures agree with the weight loss measurements that LiTFSI prevents the tBP from evaporating, because there is no uncomplexed tBP in these two samples. The limited tBP evaporation in tBP−LiTFSI can also be attributed to the coordination of the pyridine ring with a lithium ion. Thus, a synergistic effect occurs when LiTFSI and tBP are mixed and allow each other to mitigate the negative effect.

This conclusion is supported by the FTIR ring modes of the 6:1 mixture in which a peak change was observed. The "shoulder" of the 6:1 mixture FTIR peak at 1596 cm^{-1}

DOI: 10.1021/jacs.8b09809
J. Am. Chem. Soc. XXXX, XXX, XXX−XXX

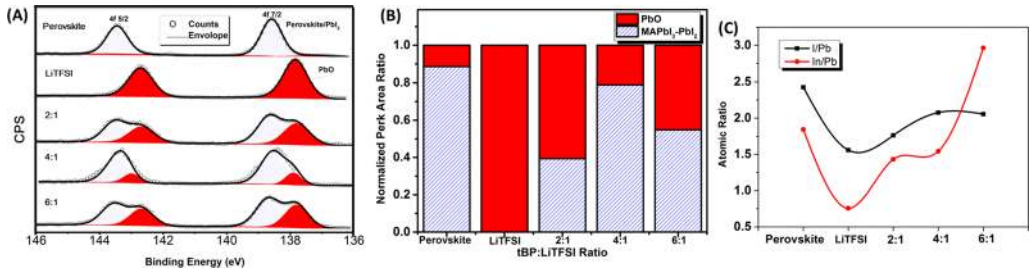

Figure 6. X-ray photoelectron spectra (XPS) of $CH_3NH_3PbI_3$ perovskite films in an ambient condition overnight which were spun with no solvent or additive, LiTFSI, and 2:1, 4:1, and 6:1 molar ratio tBP−LiTFSI mixtures, separately. (A) Pb 4f; (B) the peak area ratio for PbO to $MAPbI_3/PbI_2$ from (A); and (C) atomic ratio of In to Pb and I to Pb derived from XPS (for the XPS survey spectrum, see Supporting Information, Figure S9).

wavenumber gradually decreased. In an hour, this peak changed from a shoulder peak to a single peak. As discussed in Figure 2, the "shoulder" for this peak is attributed to the uncomplexed tBP. Therefore, the disappearance of the "shoulder" in the 6:1 mixture pyridine ring stretching peak reflects the evaporation of uncomplexed tBP. Interestingly, an increase of the peak intensity at ~1606 cm^{-1} wavenumber was observed. This is because after the tBP evaporated, the concentration of the tBP−LiTFSI complexes in the 6:1 mixture improved. The coordination of the pyridine ring with a lithium ion shows a huge impact on the properties of the tBP−LiTFSI mixtures. As a result, the formation of tBP−LiTFSI complexes limits the tBP evaporation and LiTFSI hygroscopicity. It is important to characterize whether this phenomenon can enhance the stability of the perovskite layer.

Interaction of tBP−LiTFSI Complexes with Perovskite. To investigate the influences of tBP−LiTFSI complexes on a perovskite layer, LiTFSI and the tBP−LiTFSI mixtures at different molar ratios were spun on perovskite films separately. Each sample was observed by optical microscope in an ambient condition for 240 min. Figure 5 displays the optical micrographs for $CH_3NH_3PbI_3$ films with/without HTL additives (all Figure 5 images were derived from Supporting Information Video S1 to Video S5). Three representative rows are shown in Figure 5. Row 1 is the starting time for all freshly prepared samples. Row 2 is the time when all the dark brown regions (indicative of perovskite) disappear from the samples. It can be considered as the complete degradation from perovskite to PbI_2.[50] Row 3 are the images for all the samples at 240 min.

As shown in Figure 5(A) and Supporting Information Video S1, no obvious morphological change was observed within 240 min for the perovskite sample without any HTL additives. However, in Figure 5(B) and Supporting Information Video S2, after depositing LiTFSI, the perovskite started to degrade right after finishing spin-coating (0 min), as shown in Figure 5(B). After 30 min, the perovskite film was degraded completely. Moreover, further degradation was observed, which was colorless and had a dendrite morphology after 240 min. The dendrite morphology for Figure 5(B) was observed when zoomed-out at a larger scale. (See Supporting Information Figure S7.)

According to row 2 in Figure 5(C), (D), and (E), when the perovskite layer is coated with tBP−LiTFSI mixtures, its degradation slowed down compared with the layer that was coated with only LiTFSI. The perovskite degradation time windows for samples coated with the 6:1 and 4:1 tBP−LiTFSI mixtures were 65 min. The same time window for the 2:1 tBP−LiTFSI mixture sample was 45 min. Compared with the LiTFSI-coated sample, where the time window was 30 min, introduction of tBP improved the stability of perovskite. Moreover, samples that were coated with the 6:1 and 4:1 mixtures have longer time windows than the sample coated with 2:1 mixture. This indicates that the hygroscopicities of 4:1 and 6:1 mixtures are less than that of the 2:1 mixture. The hygroscopicity difference between complexes A and B was not observed in spectroscopy measurements (Figure 3), but was elucidated from optical micrographs (Figure 5). This can be attributed to the fact that perovskite can react to a small amount of water and lead to degrade.

It is also seen that further degradation existed in row 3 of Figure 5(C) to (E) (see Supporting Information Videos S3 to S5). After the perovskite film (dark brown) has converted to PbI_2 (yellow), colorless dendrites were formed. According to Figure 5(B) (perovskite with LiTFSI), the dendrite is too large for the existing magnification of the electron microscope; hence a lower magnification is used. The size of dendrites in this sample is over 100 μm (Supporting Information Figure S7). In Figure 5(E), with the 2:1 mixture, the dendrites were reduced to ~30 μm. With the 6:1 and 4:1 mixtures, as shown in Figure 5(C) and (D), the dendrite size was further reduced to 10 μm. This trend indicates that the formation of tBP−LiTFSI complexes not only slows down the degradation from perovskite to PbI_2 but also restricts the formation of further degradation product(s).

Moreover, from Figure 5(C) to (E), some blue-colored regions showed up that were from the substrate (marked by red circles in Figure 5(C) to (E)). The samples with less coverage on the substrate showed clear evidence that the blue regions were from the substrate (see Supporting Information, Figure S8). This can be attributed to the corrosive effect of tBP to perovskite and the degradation products.[40] In Figure 5 row 3, more blue regions were observed in Figure 5(C) than (D) and (E), which supports that the existence of uncomplexed tBP in the 6:1 mixture has a more corrosive effect compared with the pure tBP−LiTFSI complexes. The optical micrograph results indicate that the 4:1 mixture maintains an optimal complex composition. This ratio prevents tBP from evaporating to induce a corrosive effect, and on the other hand, such mixture ratio reduces water uptake because Li^+ has been tightly surrounded by tBP to limit the formation of HTFSI to adsorb water (as shown in Figure 4).

Light, moisture, or oxygen can be the possible factor(s) to cause the dendrite structures to form in an ambient condition. To understand which one was the main factor for the dendrite formation, environmental scanning electron microscopy (ESEM) was applied. In ESEM, a sample was placed in a high-vacuum chamber in the dark; thus the influences of

DOI: 10.1021/jacs.8b09809
J. Am. Chem. Soc. XXXX, XXX, XXX−XXX

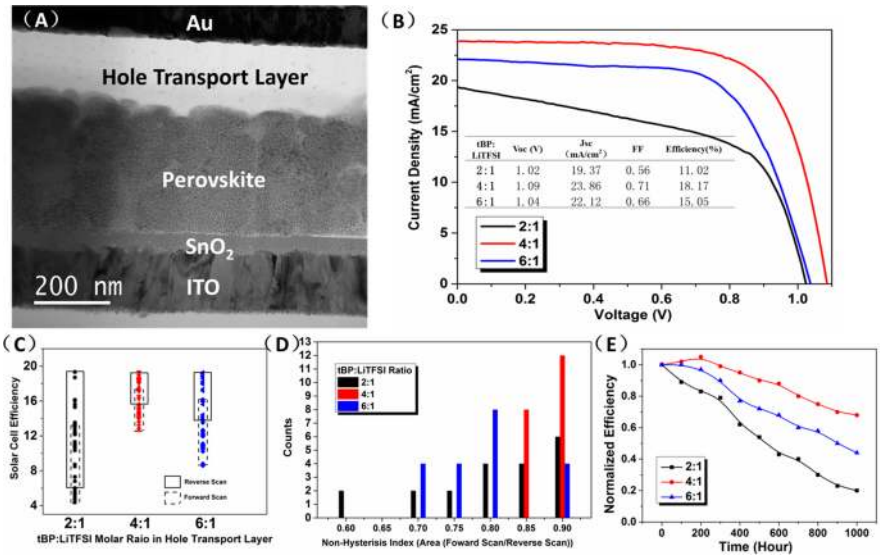

Figure 7. PSC performance results for 60 devices (20 devices for each condition) fabricated with different tBP:LiTFSI ratios. (A) Bright field transmission electron microscope (BF-TEM) cross-section image of the PSC. (B) reverse scan $J-V$ curves. Each curve is the average result for 20 devices. (C) Nonhysteresis index (the ratio of the area under the $J-V$ curve for forward scan versus reverse scan) distribution. (D) Distribution of individual device performance plotted for all 60 devices. (E) Aging curves of the devices for 1000 h in ambient condition (the aging curves are collected only from the devices over 15% efficiency at the initial measurement; all data points are the average results).

oxygen and light were ruled out. At the same time, 1.1 Tor water vapor was purged into the chamber during the observation. As shown in Figure 5(F) and Supporting Information Video S6, the dendrite formation still can be observed *in-situ* on the perovskite film with LiTFSI for 240 min under 1.1 Tor water vapor pressure in ESEM. This means that the moisture can be the primary cause of the degradation of the perovskite. It is also possible that the electron beam in ESEM may cause the dendrite formation. However, at a higher magnification as shown in Figure 5(G) and Supporting Information Video S7, the dendrites start to disappear. This means that the electron beam could not have caused the dendrite formation, but the beam actually hindered the dendrite from growing. Based on these phenomena, moisture could be the only reason to cause the perovskite to degrade more.

X-ray photoelectron spectroscopy (XPS) was applied to investigate the degradation product(s) (for survey XPS spectra, see Supporting Information, Figure S9). The chemical analysis from XPS could further support the dual effect of tBP−LiTFSI on reducing both water uptake and corrosion. Figure 6(A) displays the Pb 4f peaks for the perovskite samples spun with HTL additives, which are kept in an ambient condition overnight. A previous study shows that the Pb 4f peaks for PbI_2 and $CH_3NH_3PbI_3$ are too close to distinguish.[51] There are two pairs of peaks that are considered to get good fitting results: 138.5 and 143.4 eV, corresponding to the $4f_{7/2}$ and $4f_{5/2}$ peaks of $CH_3NH_3PbI_3/PbI_2$, respectively. Another pair is the 137.8 and 142.7 eV peaks, which are the $4f_{7/2}$ and $4f_{5/2}$ peaks for PbO, respectively.[51] It is likely that the dendrites in Figure 5 were from PbO. Figure 6(B) shows the ratio of PbO to $CH_3NH_3PbI_3/PbI_2$ according to Figure 6(A). In this figure, the perovskite film with LiTFSI has the highest amount of PbO. By introducing tBP, the amount of PbO decreased. The film with LiTFSI has almost 100% PbO, which decreased to 60% for the sample with the 2:1 tBP−LiTFSI mixture. It was further reduced to 21% and 45% for the 4:1 and 6:1 tBP−LiTFSI samples, respectively. Interestingly, the sample with the 6:1 tBP−LiTFSI mixture has higher PbO than the one with the 4:1 mixture even though the 6:1 has more tBP. This can be attributed to the uncomplexed tBP in the 6:1 sample, which dissolves $CH_3NH_3PbI_3/PbI_2$, which reduces the ratio of this component. These subsequent degradation products can make the recycling of perovskite materials more difficult: Both PbI_2 and $CH_3NH_3PbI_3$ can be recycled by polar aprotic solvents such as DMF,[52] while PbO cannot be recycled as easily. The formation of tBP−LiTFSI complexes can slow down the formation of PbO, which makes the recycling of perovskite easier. According to XPS spectra, as shown in Figure 6(C), the samples' atomic ratio of In:Pb and I:Pb can be obtained. The ratio of I:Pb is considered as the index for the perovskite degradation, because for perovskite, this ratio is 3 and 2 for PbI_2, while for PbO it is 0. This shows that with the increased amount of tBP, the samples have a higher I:Pb ratio than the perovskite film coated with pure LiTFSI. On the other hand, an indium signal occurs in the substrate ITO glass (~90% In_2O_3, 10% SnO_2); therefore the In:Pb ratio can be considered as the index for corrosive effects. It is either attributed to the tBP dissolving perovskite/PbI_2 or degradation. In this case, among the perovskite samples, which were spun with different tBP−LiTFSI mixtures, the 6:1 tBP−LiTFSI sample shows the highest In:Pb ratio. This is because of the more corrosive effect from the uncomplexed tBP to perovskite compared with the 4:1 and 2:1 tBP−LiTFSI mixtures. At the same time, the 4:1 mixture sample has less hygroscopicity compared with the 2:1 tBP−LiTFSI mixture. The XPS results of 3:1 and 5:1 mixtures also agree with the overall trend; see Supporting Information, Figure S10. All these results indicate that the 4:1 tBP−LiTFSI mixture can limit the tBP corrosive effect and restrict further degradation from pervskite/PbI_2 to PbO.

Influences of tBP−LiTFSI Complexes on Perovskite Solar Cell Performance. All physical and chemical analyses suggest that complex formation improves PSC stability. The planar PSCs[53] were fabricated to test and understand the impact of these complexes on devices. In Figure 7(A), the bright-field transmission electron microscopy (BF-TEM)

DOI: 10.1021/jacs.8b09809
J. Am. Chem. Soc. XXXX, XXX, XXX−XXX

image displays the device we fabricated. The PSCs consist of amorphous SnO_2 as a compact electron transport layer, the planar $CH_3NH_3PbI_3$ intrinsic layer, Spiro-OMeTAD, tBP and LiTFSI HTL, and gold back contact. More than 60 solar cells were fabricated in order to get statistically significant results (more than 100 solar cells were fabricated, which include 3:1 and 5:1 tBP−LiTFSI samples; see Supporting Information, Figures S11 and S12). As shown in Figure 7(B), the devices fabricated with the 4:1 tBP−LiTFSI mixture show a slightly higher performance based on the average $J-V$ curve. All devices' average $J-V$ curves with forward and reverse scans are shown in Supporting Information Figure S11. On the other hand, the 4:1 tBP−LiTFSI displayed less hysteresis from Figure 7(C). The devices' hysteresis was evaluated according to the nonhysteresis index, which is the ratio of area under the $J-V$ curve for forward scan versus reverse scan. The closer the index is to 1, the less hysteresis exists in the device. Moreover, the devices that were fabricated with the 4:1 tBP−LiTFSI mixture have less performance variation than the other two conditions. All device efficiencies are shown in Figure 7(D). Although in Figure 7(B), the 4:1 tBP−LiTFSI mixture devices show a slightly higher average performance, champion cells for all three conditions reach over 19.5% efficiency in Figure 7(C). This means that all the best devices have the capability to reach the same level no matter which tBP:LiTFSI ratio is applied. However, their variations in performance are completely different: The 4:1 tBP−LiTFSI PSCs show much less efficiency variation (standard deviation is ±1.13%, reverse scan) than the other two devices (standard deviations for 2:1 is ±4.36% and 6:1 is ±2.04%, reverse scan). The devices with 3:1 and 5:1 mixtures follow the trend as discussed (Supporting Information, Figure S12(A) and (B)). The 2:1 devices have less standard deviation than the 6:1 devices, which could indicate the LiTFSI hygroscopicity has more impact on the devices' fabrication consistence than the tBP corrosive effect. Together with the less variation of hysteresis in Figure 7(C), the 4:1 tBP−LiTFSI PSCs have much higher performance reproducibility than the other conditions. This can be attributed to the fact that the 4:1 ratio reaches the condition for reducing both corrosive and water uptake effects: it has less corrosivity to perovskite compared with the 6:1 and 5:1 samples since it does not contain uncomplexed tBP and it has lower hygroscopicity compared with the 2:1 and 3:1 samples for the less LiTFSI component.

To evaluate the impact of device stability for the tBP−LiTFSI complexes, all devices that had over 15% efficiency at the initial test were stored in a light ambient condition and tested over 1000 h. As shown in Figure 7(E), the devices that were fabricated with the 4:1 tBP−LiTFSI mixtures displayed the highest stability. For the 4:1 tBP−LiTFSI devices, the final efficiency dropped to 70% compared with the initial test, while the 2:1 tBP−LiTFSI devices dropped to 20% and the 6:1 tBP−LiTFSI devices dropped to 44%. The 3:1 and 5:1 tBP−LiTFSI devices also display worse long-term stability than the one made of 4:1 mixtures; see Supporting Information Figure S12(C). This result agrees with physical and chemical properties of the 4:1 mixture: In a device, the 4:1 tBP−LiTFSI mixture minimized the corrosivity to perovskite and has less hygroscopicity than the other two conditions. It indicates that the 6:1 tBP−LiTFSI, which is always applied in PSCs, may not be the optimized ratio; instead, the 4:1 tBP−LiTFSI shows better results with less hysteresis, higher stability, and more consistent device performances. All the differences in device performance can be correlated to how the pyridine ring coordinates with lithium ions at the molecular level.

CONCLUSION

Different tBP−LiTFSI mixtures (the tBP:LiTFSI mixtures' molar ratios were from 2:1 to 6:1) were synthesized, which displayed different physical, chemical, and spectroscopic properties. The formation of tBP−LiTFSI complexes can be attributed to pyridine ring (tBP) coordination with lithium ions (LiTFSI). Upon formation of a tBP−LiTFSI complex (A and B), both LiTFSI hygroscopicity and tBP evaporation are alleviated, which results in less water uptake, corrosion, and formation of PbO in perovskite solar cells. Our observation explains why each of the two components makes PSCs unstable, but when they are mixed at a certain ratio, the negative effects are mitigated. FTIR indicates the 4:1 tBP−LiTFSI mixture only contains complexed tBP, without uncomplexed tBP. In principle, it is a better ratio than the empirical 6:1 ratio, which is prevalent in PSC device fabrication. In practice, the 4:1 tBP−LiTFSI devices show the best average performance, enhanced stability, less hysteresis, and obviously improved performance consistency. Therefore, the 4:1 tBP−LiTFSI mixture is suggested as the "golden ratio" for PSCs: It forms a correct chemical complex to limit the negative effects of tBP and LiTFSI while maintaining the positive aspects of these materials in PSCs. It is surprising that the intermolecular behavior between the pyridine ring (tBP) and lithium ion (LiTFSI) can result in such a significant difference in the perovskite/HTL interface, finally reflected in device performance. Understanding the formation of tBP−LiTFSI complexes and their influences in perovskite solar cells can help the rational design of suitable HTL additives, which will further improve the PSCs' performance and make it one step closer to large-scale industrial fabrications.

ASSOCIATED CONTENT

Supporting Information

The Supporting Information is available free of charge on the ACS Publications website at DOI: 10.1021/jacs.8b09809.

Experimental methods for this research; summary of the tBP:LiTFSI ratio for perovskite solar cells in some reports; optical graphs of 2:1 to 6:1 tBP−LiTFSI mixtures, tBP, and LiTFSI; more detailed FTIR, optical micrographs, bonding mechanism, XPS, and $J-V$ curves (PDF)

Optical micrograph video for the perovskite in ambient conditions for 4 h (AVI)

Optical micrograph video for the perovskite coated with LiTFSI in ambient conditions for 4 h (AVI)

Optical micrograph video for the perovskite coated with 6:1 tBP−LiTFSI in ambient conditions for 4 h (AVI)

Optical micrograph video for the perovskite coated with 4:1 tBP−LiTFSI in ambient conditions for 4 h (AVI)

Optical micrograph video for the perovskite coated with 2:1 tBP−LiTFSI in ambient conditions for 4 h (AVI)

ESEM video for the perovskite coated with LiTFSI in a 1.1 Torr water vapor pressure for 4 h at large scale (AVI)

ESEM video for the perovskite coated with LiTFSI in a 1.1 Torr water vapor pressure for 4 h at small scale (AVI)

DOI: 10.1021/jacs.8b09809
J. Am. Chem. Soc. XXXX, XXX, XXX−XXX

AUTHOR INFORMATION

Corresponding Authors

*w2xiong@ucsd.edu
*shirleymeng@ucsd.edu

ORCID

Shen Wang: 0000-0003-3826-4397
Xuefeng Wang: 0000-0001-9666-8942
Yingmin Li: 0000-0001-6383-8175
Wei Xiong: 0000-0002-7702-0187
Ying Shirley Meng: 0000-0001-8936-8845

Notes

The authors declare no competing financial interest.

ACKNOWLEDGMENTS

S.W., S.V., P.P., and Y.S.M. are grateful for the financial support from the California Energy Commission EPIC Advance Breakthrough award (EPC-16-050). Y.L. and W.X. thank the financial support from Air Force Office of Scientific Research Young Investigator Program award (FA9550-17-1-0094). The XPS and TEM work were performed at the University of California, Irvine Materials Research Institute (IMRI), using instrumentation funded in part by the National Science Foundation Major Research Instrumentation Program under Grant CHE-1338173. FIB, ESEM, and optical microscopy were performed at the San Diego Nanotechnology Infrastructure (SDNI), a member of the National Nanotechnology Coordinated Infrastructure, which is supported by the National Science Foundation (Grant ECCS-1542148).

REFERENCES

(1) Kim, H. S.; Lee, C. R.; Im, J. H.; Lee, K. B.; Moehl, T.; Marchioro, A.; Moon, S. J.; Humphry-Baker, R.; Yum, J. H.; Moser, J. E.; Grätzel, M.; Park, N. G. *Sci. Rep.* **2012**, *2*, 591.

(2) Wei, H.; Fang, Y.; Mulligan, P.; Chuirazzi, W.; Fang, H. H.; Wang, C.; Ecker, B. R.; Gao, Y.; Loi, M. A.; Cao, L.; Huang, J. *Nat. Photonics* **2016**, *10*, 333−339.

(3) Kojima, A.; Teshima, K.; Shirai, Y.; Miyasaka, T. *J. Am. Chem. Soc.* **2009**, *131*, 6050−6051.

(4) Tan, Z.-K.; Moghaddam, R. S.; Lai, M. L.; Docampo, P.; Higler, R.; Deschler, F.; Price, M.; Sadhanala, A.; Pazos, L. M.; Credgington, D.; Hanusch, F.; Bein, T.; Snaith, H. J.; Friend, R. H. *Nat. Nanotechnol.* **2014**, *9*, 687−692.

(5) Sutherland, B. R.; Sargent, E. H. *Nat. Photonics* **2016**, *10*, 295−302.

(6) Im, J.-H.; Lee, C.-R.; Lee, J.-W.; Park, S.-W.; Park, N.-G. *Nanoscale* **2011**, *3*, 4088−4093.

(7) Liu, M.; Johnston, M. B.; Snaith, H. J. *Nature* **2013**, *501*, 395−398.

(8) Burschka, J.; Pellet, N.; Moon, S.-J.; Humphry-Baker, R.; Gao, P.; Nazeeruddin, M. K.; Grätzel, M. *Nature* **2013**, *499*, 316−320.

(9) Lee, M. M.; Teuscher, J.; Miyasaka, T.; Murakami, T. N.; Snaith, H. J. *Science* **2012**, *338*, 643−647.

(10) NREL Efficiency Chart. http://www.nrel.gov/ncpv/images/efficiency_chart.jpg (accessed Jul 30, 2018).

(11) Marchioro, A.; Teuscher, J.; Friedrich, D.; Kunst, M.; van de Krol, R.; Moehl, T.; Grätzel, M.; Moser, J.-E. *Nat. Photonics* **2014**, *8*, 250−255.

(12) Xu, X.; Chen, Q.; Hong, Z.; Zhou, H.; Liu, Z.; Chang, W. H.; Sun, P.; Chen, H.; Marco, N. De; Wang, M.; Yang, Y. *Nano Lett.* **2015**, *15*, 6514−6520.

(13) Ergen, O.; Gilbert, S. M.; Pham, T.; Turner, S. J.; Tan, M. T. Z.; Worsley, M. A.; Zettl, A. *Nat. Mater.* **2017**, *16*, 522−525.

(14) Ono, L. K.; Juarez-Perez, E. J.; Qi, Y. *ACS Appl. Mater. Interfaces* **2017**, *9*, 30197−30246.

(15) Nguyen, W. H.; Bailie, C. D.; Unger, E. L.; McGehee, M. D. *J. Am. Chem. Soc.* **2014**, *136*, 10996−11001.

(16) Liu, Y.; Chen, Q.; Duan, H.-S.; Zhou, H.; Yang, Y.; Chen, H.; Luo, S.; Song, T.-B.; Dou, L.; Hong, Z.; Yang, Y. *J. Mater. Chem. A* **2015**, *3*, 11940−11947.

(17) Leijtens, T.; Giovenzana, T.; Habisreutinger, S. N.; Tinkham, J. S.; Noel, N. K.; Kamino, B. A.; Sadoughi, G.; Sellinger, A.; Snaith, H. J. *ACS Appl. Mater. Interfaces* **2016**, *8*, 5981−5989.

(18) Ma, S.; Zhang, H.; Zhao, N.; Cheng, Y.; Wang, M.; Shen, Y.; Tu, G. *J. Mater. Chem. A* **2015**, *3*, 12139−12144.

(19) Zhang, J.; Xu, B.; Yang, L.; Mingorance, A.; Ruan, C.; Hua, Y.; Wang, L.; Vlachopoulos, N.; Lira-Cantú, M.; Boschloo, G.; Hagfeldt, A.; Sun, L.; Johansson, E. M. J. *Adv. Energy Mater.* **2017**, *7*, 1602736−1602743.

(20) Jeon, N. J.; Na, H.; Jung, E. H.; Yang, T. Y.; Lee, Y. G.; Kim, G.; Shin, H. W.; Il Seok, S.; Lee, J.; Seo, J. *Nat. Energy* **2018**, *3*, 682−689.

(21) Heo, J. H.; Im, S. H.; Noh, J. H.; Mandal, T. N.; Lim, C. S.; Chang, J. A.; Lee, Y. H.; Kim, H. J.; Sarkar, A.; Nazeeruddin, M. K.; Grätzel, M.; Seok, S. *Nat. Photonics* **2013**, *7*, 486−491.

(22) Jeon, N. J.; Noh, J. H.; Kim, Y. C.; Yang, W. S.; Ryu, S.; Seok, S., II *Nat. Mater.* **2014**, *13*, 897−903.

(23) Christians, J. A.; Fung, R. C. M.; Kamat, P. V. *J. Am. Chem. Soc.* **2014**, *136*, 758−764.

(24) Arora, N.; Dar, M. I.; Hinderhofer, A.; Pellet, N.; Schreiber, F.; Zakeeruddin, S. M.; Grätzel, M. *Science* **2017**, *358*, 768−771.

(25) Wijeyasinghe, N.; Regoutz, A.; Eisner, F.; Du, T.; Tsetseris, L.; Lin, Y. H.; Faber, H.; Pattanasattayavong, P.; Li, J.; Yan, F.; McLachlan, M. A.; Payne, D. J.; Heeney, M.; Anthopoulos, T. D. *Adv. Funct. Mater.* **2017**, *27*, 1701818−1701830.

(26) You, J.; Meng, L.; Song, T.-B.; Guo, T.-F.; Yang, Y.; Chang, W.-H.; Hong, Z.; Chen, H.; Zhou, H.; Chen, Q.; Liu, Y.; De Marco, N.; Yang, Y. *Nat. Nanotechnol.* **2016**, *11*, 1−8.

(27) Yang, W. S.; Park, B. W.; Jung, E. H.; Jeon, N. J.; Kim, Y. C.; Lee, D. U.; Shin, S. S.; Seo, J.; Kim, E. K.; Noh, J. H.; Seok, S., II *Science* **2017**, *356*, 1376−1379.

(28) Yang, W. S.; Noh, J. H.; Jeon, N. J.; Kim, Y. C.; Ryu, S.; Seo, J.; Seok, S., II *Science* **2015**, *348*, 1234−1237.

(29) Wang, S.; Yuan, W.; Meng, Y. S. *ACS Appl. Mater. Interfaces* **2015**, *7*, 24791−24798.

(30) Yuan, W.; Zhao, H.; Hu, H.; Wang, S.; Baker, G. L. *ACS Appl. Mater. Interfaces* **2013**, *5*, 4155−4161.

(31) Wang, S.; Sina, M.; Parikh, P.; Uekert, T.; Shahbazian, B.; Devaraj, A.; Meng, Y. S. *Nano Lett.* **2016**, *16*, 5594−5600.

(32) Habisreutinger, S. N.; Noel, N. K.; Snaith, H. J.; Nicholas, R. J. *Adv. Energy Mater.* **2017**, *7*, 1601079−1601086.

(33) Juarez-Perez, E. J.; Leyden, M. R.; Wang, S.; Ono, L. K.; Hawash, Z.; Qi, Y. *Chem. Mater.* **2016**, *28*, 5702−5709.

(34) Chen, B. A.; Lin, J. T.; Suen, N. T.; Tsao, C. W.; Chu, T. C.; Hsu, Y. Y.; Chan, T. S.; Chan, Y. T.; Yang, J. S.; Chiu, C. W.; Chen, H. M. *ACS Energy Lett.* **2017**, *2*, 342−348.

(35) Wang, S.; Jiang, Y.; Juarez-Perez, E. J.; Ono, L. K.; Qi, Y. *Nat. Energy* **2017**, *2*, 16195−16202.

(36) Wang, Q.; Chen, B.; Liu, Y.; Deng, Y.; Bai, Y.; Dong, Q.; Huang, J. *Energy Environ. Sci.* **2017**, *10*, 516−522.

(37) Divitini, G.; Cacovich, S.; Matteocci, F.; Cinà, L.; Di Carlo, A.; Ducati, C. *Nat. Energy* **2016**, *1*, 15012−15017.

(38) Aristidou, N.; Eames, C.; Sanchez-Molina, I.; Bu, X.; Kosco, J.; Islam, M. S.; Haque, S. A. *Nat. Commun.* **2017**, *8*, 15218−15227.

(39) Bao, Q.; Liu, X.; Braun, S.; Fahlman, M. *Adv. Energy Mater.* **2014**, *4*, 1301272−1301278.

(40) Li, W.; Dong, H.; Wang, L.; Li, N.; Guo, X.; Li, J.; Qiu, Y. *J. Mater. Chem. A* **2014**, *2*, 13587−13592.

(41) Xi, H.; Tang, S.; Ma, X.; Chang, J.; Chen, D.; Lin, Z.; Zhong, P.; Wang, H.; Zhang, C. *ACS Omega* **2017**, *2*, 326−336.

(42) Dong, G.; Xia, D.; Yang, Y.; Shenga, L.; Ye, T.; Fan, R. *ACS Appl. Mater. Interfaces* **2017**, *9*, 2378−2386.

(43) Burschka, J.; Dualeh, A.; Kessler, F.; Baranoff, E.; Cevey-Ha, N. L.; Yi, C.; Nazeeruddin, M. K.; Grätzel, M. *J. Am. Chem. Soc.* **2011**, *133*, 18042−18045.

DOI: 10.1021/jacs.8b09809
J. Am. Chem. Soc. XXXX, XXX, XXX−XXX

(44) Liang, H.; Li, H.; Wang, Z.; Wu, F.; Chen, L.; Huang, X. *J. Phys. Chem. B* **2001**, *105*, 9966−9969.
(45) Fulfer, K. D.; Kuroda, D. G. *J. Phys. Chem. C* **2016**, *120*, 24011−24022.
(46) Lee, K. K.; Park, K.; Lee, H.; Noh, Y.; Kossowska, D.; Kwak, K.; Cho, M. *Nat. Commun.* **2017**, *8*, 14658.
(47) Yurdakul, S.; Bahat, M. *J. Mol. Struct.* **1997**, *412*, 97−102.
(48) Jones, L. H. *J. Chem. Phys.* **1954**, *22*, 217−219.
(49) Foropoulos, J., Jr; DesMarteau, D. D. *Inorg. Chem.* **1984**, *23*, 3720−3723.
(50) Habisreutinger, S. N.; Leijtens, T.; Eperon, G. E.; Stranks, S. D.; Nicholas, R. J.; Snaith, H. J. *Nano Lett.* **2014**, *14*, 5561−5568.
(51) Huang, W.; Manser, J. S.; Kamat, P. V.; Ptasinska, S. *Chem. Mater.* **2016**, *28*, 303−311.
(52) Kim, B. J.; Kim, D. H.; Kwon, S. L.; Park, S. Y.; Li, Z.; Zhu, K.; Jung, H. S. *Nat. Commun.* **2016**, *7*, 11735−11743.
(53) Zhang, D.; Cui, B.-B.; Zhou, C.; Li, L.; Chen, Y.; Zhou, N.; Xu, Z.; Li, Y.; Zhou, H.; Chen, Q. *Chem. Commun.* **2017**, *53*, 10548−10551.

DOI: 10.1021/jacs.8b09809
J. Am. Chem. Soc. XXXX, XXX, XXX−XXX